Ultra-long multicolor belts and unique morphologies of tin-doped zinc oxide nanostructures

S. Zia · M. Amin · U. Manzoor · A.S. Bhatti

Abstract We demonstrate the synthesis, characterization and application of pure and tin (Sn) doped zinc oxide (ZnO) nanostructures with unique optical properties. Pencil-shaped nanorods were synthesized using a mixture of pure ZnO and carbon as starting material. The growth mechanism of these nanorods is discussed in detail. Sn-doped ultra-long belt-shape ZnO structures show many different colors in a single belt under fluorescent light in an optical microscope. These different colors are attributed to the presence of different defects in the ZnO lattice. X-ray diffraction and UV–VIS spectroscopy results are in good agreement with each other. A major application for these belts is likely to be in a single-particle sensor. A single belt based UV sensor is also fabricated and the results suggest that these photoconducting belts can serve as highly sensitive UV-light detectors.

1 Introduction

Oxides are the basis of smart and functional materials [1]. Device fabrication and synthesis using oxide semiconductors have become more important recently because physical properties of these oxides can be tuned. Among oxide semiconductors, ZnO has wide band gap energy (3.37 eV at room temperature), large exciton binding energy (60 meV) and strong piezoelectric and optical properties [2]. Nanostructured ZnO materials have attracted attention as promising candidates for future electro-optic devices.

One-dimensional (1-D) ZnO nanostructures can be synthesized by numerous synthesis techniques such as electrochemical and vapor transport methods and liquid-phase techniques [3–7]. Among these, the vapor transport method is one of the most extensively explored approaches due to single crystallinity and high aspect ratio of nanostructures. The growth kinetic of ZnO nanostructures obtained by the vapor transport method depends on many factors, i.e. activation energy of crystallization, radius of catalyst droplet, supersaturation, synthesis temperature, volume of liquid droplet and the equilibrium vapor pressure of the system [8].

Different morphologies of ZnO nanostructures, i.e. nanobelts [2], nanowires [9], nanotubes [10], nanosheets [11] and nanocombs [12] etc, have been fabricated. Doping of these nanostructures has also been reported and the success of doping is often accompanied and characterized by changes in optical, electrical and/or structural properties of ZnO nanostructures [13]. These ZnO nanostructures serve as cantilevers, resonators, optical sensors, solar cells and electrodes and are also considered as the best material for fabrication of UV light emitting diodes and nanolasers at room temperature. They show piezoelectricity because of the lack of symmetry in wurtzite structure [14]. ZnO nanostructures also have large numbers of extrinsic and intrinsic deep-level impurities which emit light of different colors [15].

In recent studies, the relationship between defect chemistry and optical properties of ZnO is of particular interest and many independent research groups have studied it in detail and supported the relation with experimental results

S. Zia · M. Amin · U. Manzoor (✉) · A.S. Bhatti
Centre for Micro & Nano Devices, Department of Physics,
COMSATS Institute of Information Technology, Islamabad,
Pakistan
e-mail: umanzoor@comsats.edu.pk

U. Manzoor
Alamoudi Water Chair, King Saud University, Riyadh, Kingdom
of Saudi Arabia
e-mail: umanzoor@ksu.edu.sa

and theoretical modeling. It was reported that the band gap of ZnO can also be fine tuned by doping [16].

In this study we have systematically controlled the morphology by controlled doping of Sn by the vapor transport method. Ultra-long Sn-doped belts show different colors, in the visible range, under fluorescent light. A single belt based UV sensor was also fabricated and tested for different UV intensities.

2 Experimental procedure

ZnO nanostructures were synthesized by the vapor transport method. Equal amounts (by weight) of ZnO powder (99.0 %, Hayashi Pure Chemical Industries, Osaka, Japan) and carbon black were mixed and milled in a planetary ball mill (Fritsch, Germany) for 25 h at 200 rpm. Si (100) p-type substrates were dip coated in a dilute solution of extensively milled ZnO and methanol at room temperature and dried in air for 30 min. 1.0 g starting material was carefully weighed and loaded into an alumina boat. ZnO-coated substrates were placed at the top of the boat using carbon tape. The boat was then placed at the center of a quartz tube furnace ($\varnothing$ 52 mm). One end of the tube was attached to an Ar cylinder through a mass flow controller. The other end of the tube was left open for oxygen supply. The temperature, dwell time and Ar flow rate were 950 °C, 1.5 h and 30 sccm, respectively.

0.1 and 0.2 g SnO respectively were mixed in 1.0 g of starting mixture using a mortar and pestle for the doped samples. A pure ZnO sample (S0), a sample with 0.1 g SnO (S1) and a sample with 0.2 g SnO (S2) were prepared.

A scanning electron microscope (SEM, model: Hitachi SU-1500) was used to study the morphology of nanostructures. Crystal structure and phase purity of as-grown products were characterized by X-ray diffraction (XRD, model: PANalytical X-pert Pro with Cu-Kα radiation). Optical properties were measured using UV–VIS spectroscopy and an optical microscope (Olympus BX61).

3 Results and discussion

Figure 1 shows the SEM images of S0, S1 and S2 nanostructures. Morphology of S0 (Fig. 1a) is mostly hexagonal (pencil-shaped) nanostructures with a clearly defined hexagonal rod and a sharp tip. The diameter along the length is continuously decreasing towards the tip. The average diameter of the hexagonal rods (from the middle) is 1.40 ± 0.46 μm and the diameter of the tip is less than 80 nm. These pencil-shaped nanostructures are a typical example of hexagonal structures grown in near-thermodynamical conditions.

The growth mechanism of these oxide crystals is complex. Figure 1b is a schematic illustration of the proposed growth mechanism from a kinetics point of view. The nuclei were formed on the milled ZnO nanoparticle by heterogeneous nucleation (minimum-energy requirement). The crystal growth was achieved by incorporation of growth units on to the nuclei, generated from the starting mixture in the form of vapors (Fig. 1b(ii)). In the beginning, the structure grew under near-thermodynamical conditions. The vapors produced from the starting mixture were not meeting the optimum requirements, but in the beginning the deposited vapors were enough to maintain the overall hexagonal structure. At the later stage, with the depletion of vapors the *c*-axis grew at a very fast rate giving it a needle-shaped morphology. The growth interface of ZnO crystals is established on the basis of an ideal growth mechanism, which considers the interface structure of the crystal as the stacking order of coordination polyhedrons with Zn^{+2} or O^{-2} ions. It is generally accepted that ZnO has different growth rates for different crystal directions. For example, the (0001) plane is the most unstable and therefore the fastest growing plane as the number of broken bonds per unit area is highest (according to broken-bond theory). Low-indexed planes have slower growth rates than (0001) and stable planes have the slowest growth rates (sides of the hexagon) [17].

During the growth phase, the vapors deposit in a systematic manner but, after some time, the vapors start depleting because of an insufficient amount of the starting mixture. The direct effect of this fact was the decrease in the overall diameter of the pencil-shaped structures. In the last phase, experimental parameters along with depleted vapors were combined in such a way that *c*-axis growth was very fast to form a needle-shaped structure (surface instability). It is expected that the depletion of vapors by carefully controlling the amount of starting mixture plays a major role in the formation of pencil-shaped structures. Our previous reported results clearly suggest flat-tip rods when the supply of vapors from the source mixture is infinite throughout the experiment [7].

Systematic experimental results with variable starting mixture quantity (not reported here) suggested that final tips were formed when the amount of starting mixture was not enough. Another clear indication of depleted vapors was the white color of the remaining mixture in the boat. If the quantity of starting mixture is more than 1.2 g, the remaining mixture had either a grey or a blackish-gray color, clearly indicating the presence of unreacted carbon.

The typical top view of as-deposited morphologies of doped ZnO nanostructures is shown in Fig. 1c–e. The images clearly suggest presence of mixed morphologies of nanowires and needle-like belt-shape structures with low dopant levels (sample S1, Fig. 1c–e). The length and diameter of nanowires are 8.87 ± 0.66 μm and 114 ± 43 nm, respectively (Fig. 1c). Needle-like belt-shape structures with
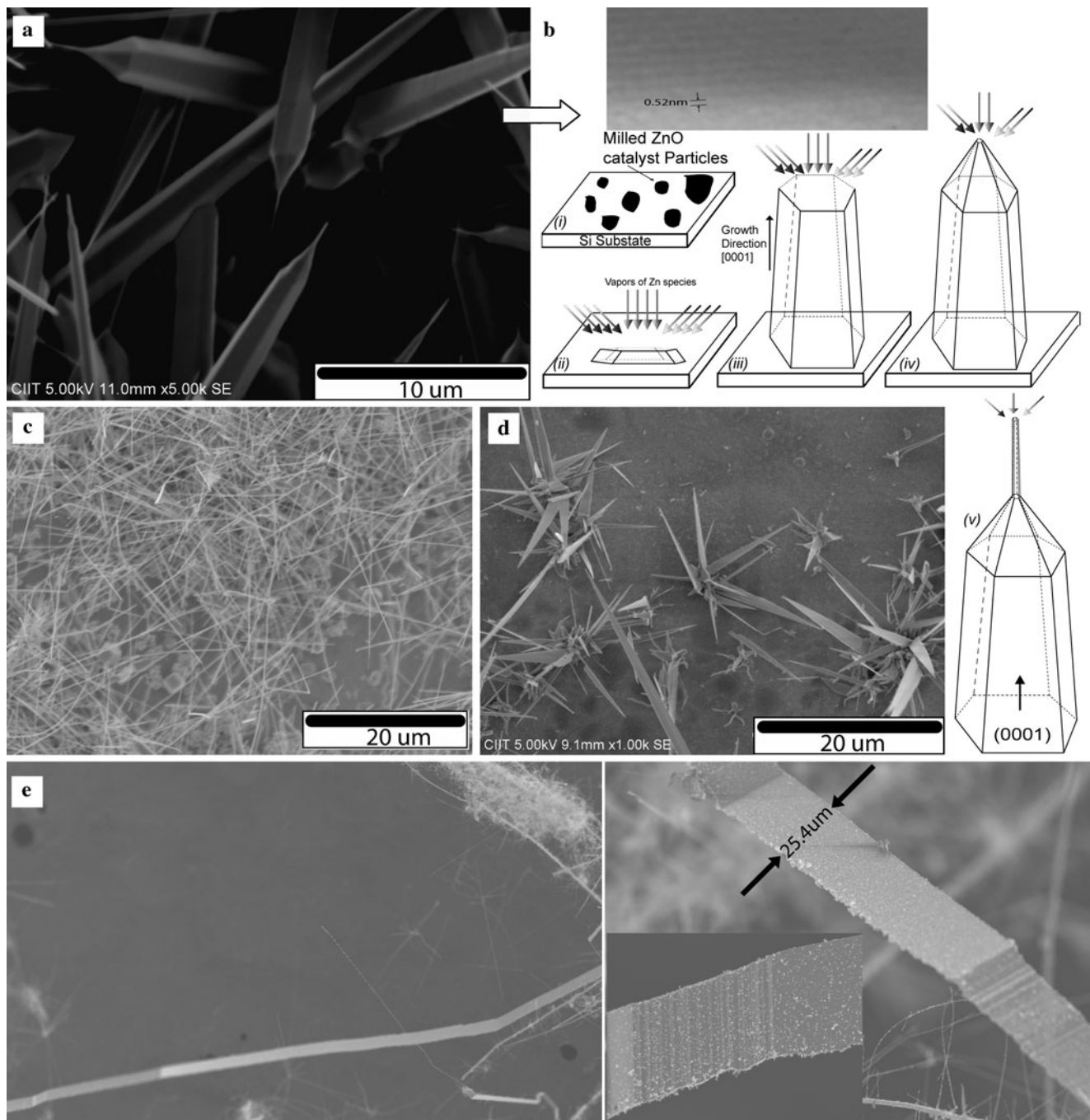
Fig. 1 SEM images of doped and undoped samples. (**a**) Unique pencil-shaped nanostructures with sharp tips were formed for S0. (**b**) Schematic diagram of the proposed growth mechanism of pencil-shaped nanostructures. The *inset* is the HRTEM image of the tip, suggesting the *c*-axis as the growth direction. (**c, d**) Mixed morphologies (nanowires and needle-like belt-shape structures) were formed on the same substrate for S1. (**e**) Low-magnification SEM image of ultra-long belt-shape structures for S2. The *inset* is a higher magnification image confirming belt-shape morphology

length 42.1 ± 4.2 μm and tip diameter 418 ± 86 nm are also present on the same substrate (Fig. 1d). These needle-like belt-shape structures resemble a famous cactus plant Agave Americana, i.e. a spreading rosette originating from one point. Ultra-long belts (sample S2, Fig. 1e) were formed with higher doping levels. The length of these ultra-long belts is ≥ 400 μm with a width of 25.2 ± 9.8 μm. The two insets in the figure clearly suggest a belt-shape structure with well-defined edges. The growth mechanism for belt-shape structures has been reported [18] but it lacks compelling thermodynamics and kinetics explanations, so carefully designed experiments are needed to further clarify the theory.
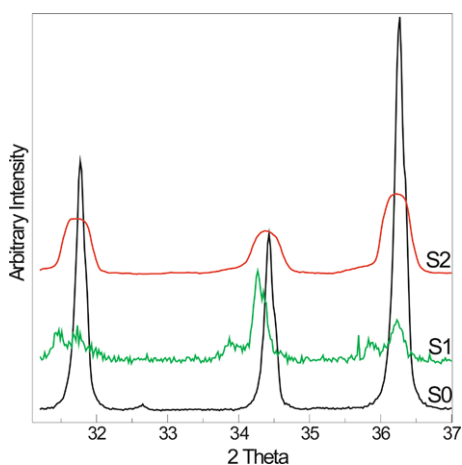
Fig. 2 XRD results of doped and undoped ZnO samples. Shifts in the main peaks and broader FWHMs after increase in SnO doping clearly suggest increase in defect concentration

Fig. 3 Room-temperature transmittance spectra of S0, S1 and S2. The results clearly suggest wider direct band emission with increase in doping. Peak intensities and positions of defect-related peaks are different for different samples, suggesting different defects and/or concentrations for different samples

The X-ray diffraction spectra of pure and doped ZnO nanostructures are shown in Fig. 2. Diffraction peaks clearly suggest phase-pure ZnO. The XRD results clearly suggest peak broadening with increase in Sn concentration. The full widths at half-maximum (FWHMs) for pure ZnO nanostructures are narrower than those for doped samples, clearly indicating good crystallinity. Presence of dopants in a crystal lattice is a complex issue and depends on amount and type of dopant, position in the crystal lattice, size and oxidation states etc. In our case it is expected that Sn can present as either Sn^{2+} or Sn^{4+} in the crystal lattice and in both the cases the ionic radii are slightly different than Zn^{2+}, causing the lattice to expand. This peak broadening may also be ascribed to a smaller crystallite size and a larger strain due to more defect formations, such as point defects, dislocations and stacking faults, etc. [19]. However, the effect of crystal size and/or strain cannot be resolved from limited XRD diffraction peaks, due to the strong preferred orientations of the nanostructures. The above-mentioned effect can also be one of the possible reasons for the change in morphology by doping. Another possible reason for change in morphology by doping can be the adatom diffusion [20]. It is known that the higher the melting points of the bulk materials, the slower is the adatom diffusion. Growth morphology is the result of the competition of the diffusion process. Different materials have different diffusion coefficients, resulting in crystal defects and stress etc. and therefore resulting in different morphologies. More in-depth knowledge of the kinetics and new experimental techniques are required to completely understand morphology change with doping.

The UV-spectroscopy transmission data at room temperature for all the samples are shown in Fig. 3. The lines are uniform indicating that light is not scattered by a rough surface or inhomogeneous material and overall signal to noise
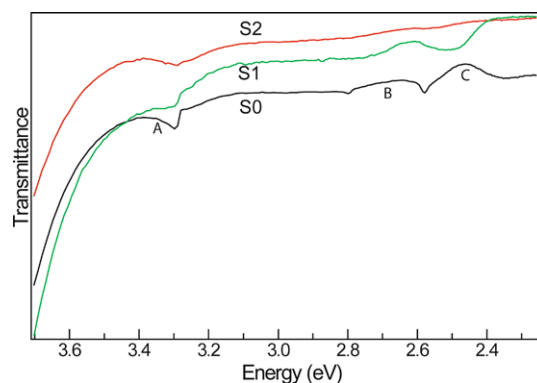
ratio is good. There are three major peaks in the spectra. Peak 'A' is in the UV range and the sharpness decreases significantly for doped samples. The optical band gap widens progressively with Sn doping. This is explained by Sernelius et al. [21] using an effective mass model. It is expected that dopant atoms enter substitutionally into the zinc sites in the ZnO lattice so that they act as ionized donors (different oxidation states). Therefore, it is likely to be associated with oxygen deficiencies. As it is doped more and more, the donor electrons occupy the states at the bottom of the conduction band (C.B.). This results in a band gap widening described by a well-known Burstein–Moss shift (blue shift) [22]. Therefore, the overall modification and suppression of emission are possibly because of the modified densities of photonic states due to the presence of Sn. Similarly, there is a systematic shift in the peak towards higher energy. Phonon broadening appears to be the dominant broadening mechanism, since the sharpness of the exciton peak degrades dramatically with doping. The broadening due to Sn obscures the details of the individual excitons, but the net influence on the absorption spectra is still extremely significant.

The three valence bands (V.B.s) of wurtzite semiconductors are non-degenerate and result in the formation of the excitons labeled in order of the valence bands as 'A', 'B' and 'C'. In the case of ZnO, it is important to note that the valence band structure differs from that of other II–VI and III–V wurtzite semiconductors because the spin–orbit coupling is negative [23]. Also, band gaps below 3.2 eV (peaks B and C) can be due to different defects. These defects results in existence of a valence band–donor transition which can dominate the absorption spectrum [24].

Native or intrinsic defects are imperfections in the crystal lattice that involve only the constituent elements. Understanding the incorporation and behavior of point defects in ZnO is essential to its successful application in semiconduc-
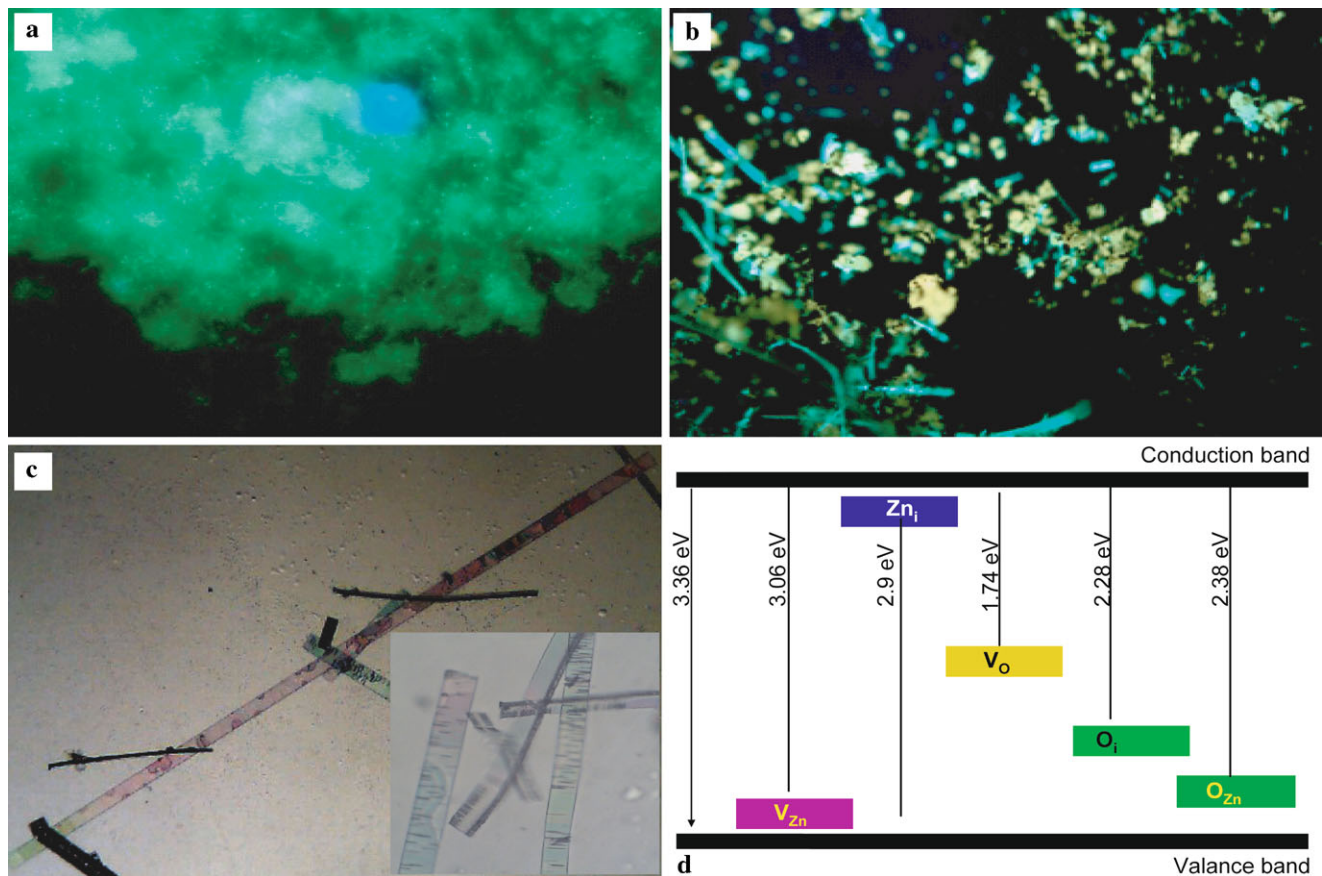
Fig. 4 (**a**) Fluorescent image of sample S0, clearly showing an overall *green* color. (**b**) Fluorescent image of sample S1. *Green* and *yellow* colors are clearly visible, suggesting change in defect density as compared to S0. (**c**) Fluorescent image of a single belt of sample S2. The image clearly shows different colors along the length of the belt. The *inset* is the higher magnification image of different belts with different colors

tor devices. Defects are often electrically active and introduce levels in the band gap of the semiconductor, which involve transitions between different charge states of the same defect [25, 26] and these transition levels are observable quantities that can be derived and estimated. Optical microscopy (fluorescence) images of ZnO nanostructures with different compositions are shown in Fig. 4. Crystal defects in S0 (pure ZnO) produce an overall green color (wavelength ≈530 nm) because of modified densities of photonic states. This overall green color suggests similar defect types and concentrations in all the nanostructures. The defect formation energies depend largely on the atomic chemical potentials. The defects associated with oxygen excess, i.e. the zinc vacancy, the oxygen interstitials and the oxygen anti-site, increase defect formation energies, whereas those associated with zinc excess, i.e. the oxygen vacancy, the zinc interstitials and the zinc anti-site, have lower defect formation energies (in Zn-rich environment). Among the defects associated with oxygen excess, the zinc vacancy exhibits the lowest formation energy [27]. This lowest formation energy suggests that the defect density of V_{Zn} is highest and, in our opinion,

is the reason for the common green color of a defective ZnO crystal under UV light.

Fluorescence images of S1 (Fig. 4b) show mainly yellow and green colors for individual nanostructures, suggesting that the presence of Sn changes the types of defects and/or defect concentrations in the ZnO crystal lattice. From the suggested band gap diagram (Fig. 4d), it is clear that oxygen-related defects may increase with Sn doping, giving it a yellow color.

Very interesting results were obtained when S2 nanostructures were observed under the fluorescent light (Fig. 4c). Many different colors are seen in a single belt and the color changes along the length of these belts. It is established that by changing the point defect density (in this case achieved by Sn doping), the optical absorption at long wavelengths (400–700 nm) is drastically altered. For S2, the visible emission colors due to defects are violet, green, orange, red and yellow. The green emission has already been discussed. For red emission, the transition is from Zn_i to the valence band in the transmission graph, also providing proof of Zn interstitials. Violet emission (at ≈400 nm) is responsible for the

Table 1 Summary and comparison (with Ref. [16]) of reported and selected experimental results for the observed colors for 1st order transitions in ZnO

Emission color	Deep-level transition (theoretical values) [16]	Deep-level transition (selected experimental values)
Violet	Zn interstitial to V.B. (0.05 eV), (0.5 eV), (0.46 eV)	3.14 eV (S1), 3 eV (S2)
Green	C.B. to O vacancy or to Zn vacancy, C.B. to both O vacancy and Zn vacancy (1.62 eV), (2.3 eV)	2.27 eV (S0), 2.31 eV (S1)
Yellow	C.B. to O interstitial (2.28 eV)	Colors observed but not enough resolution in transmission spectra
Orange	C.B. to O interstitial or Zn interstitial to O interstitial (2.96 eV)	Colors observed but not enough resolution in transmission spectra
Red	Lattice disorder along *c*-axis	1.94 eV (S0), 1.87 eV (S1), 1.88 and 1.93 eV (S2)

deep-level transition from the conduction band to V_{Zn}. The related defects for other colors have been summarized in Table 1 with comparison of theoretical and experimental values. However, it is important to note that only 1st order transitions are discussed here. The defect-related visible light emissions can also occur from higher order transitions in a much more complex manner. Another issue in ZnO is that transition levels and formation energies are calculated with a large uncertainty, resulting in the underestimation of the band gap of ZnO by 75 % [28]. These transitions are also dependent on the stresses and strains in the crystal. Therefore, transition levels related to defects that induce states in the band gap can be significantly underestimated and the schematics shown in Fig. 4d may only be used for comparison purposes and not as absolute values. This area is still open for theoretical and experimental researches.

XRD and UV–VIS spectroscopy and optical florescence results are in perfect agreement with each other. Steeper slopes in UV and lower XRD intensities suggest decrease in the crystal defects and improving quality of ZnO. The XRD peak shift also indicates a change in *d* spacing with a change in Sn doping concentration, which can be related to defect type and concentration.

Figure 5 shows the response of on–off cycles of UV illumination on a single belt of S2. The sensing mechanism of ZnO-based optical sensors relies on change in electrical conductivity as a result of photoconductivity and is responsible for decrease in resistance on illumination with UV light. The experiment was performed by a two-probe method at room temperature. Figure 5 (inset) shows the optical microscopy image of the actual sensor made from a single belt of S2. The contacts were made by putting small droplets of silver paste on both ends of the belt and drying at 60 °C. The result of UV sensing clearly suggests that electrical resistance decreases when the UV source is 'on' and vice versa. This overall change is because of the photoconduction. In the beginning of the experiment, the distance between the lamp and the sample was 20 cm and the distance was reduced to 10 cm in the last two cycles. The change in the
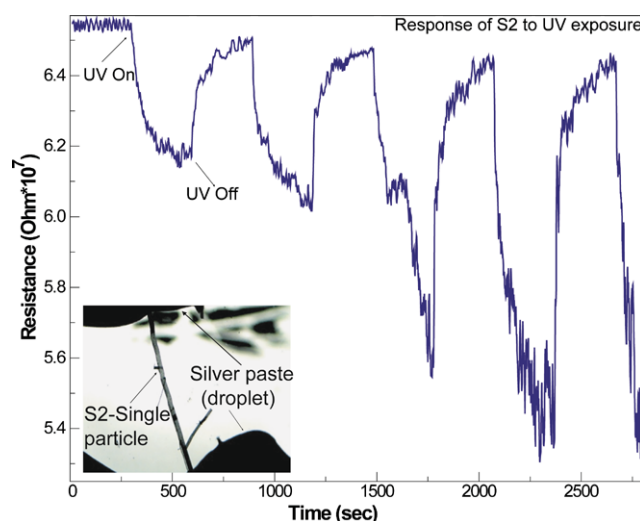

Fig. 5 Cyclic response of single belt of S2 to UV light. In the first two cycles, the distance between the sensor and the UV source was 20 cm. The distance was only 10 cm for the last two cycles. The results clearly suggest decrease in resistance on illumination with the UV lamp (photoconductivity). The *inset* is the optical microscopy image of the belt and the *black spots* are the silver paste

latter case is much more due to increase in the number of active photons for photoconduction. Soci et al. have proposed that the highly sensitive UV detection of ZnO nanowires is due to the presence of oxygen-related hole-trapping states at the nanowire surface [29]. Suehiro et al. reported a similar response with ZnO nanowires and the results are comparable with our results [30]. These photoconducting belts could serve as highly sensitive UV-light detectors, chemical and biological sensors and switching devices for nanoscale optoelectronic applications, where the binary states can be addressed optically.

4 Conclusion

We demonstrated that ZnO morphology can be controlled by carefully controlling Sn doping concentration in the vapor

transport method. The possible reasons can be adatom diffusion and/or different defects due to doping. X-ray diffraction revealed broadening of FWHM and shifting of peak position with increase in doping concentration, suggesting increase in defect concentration and change in d spacing, respectively. UV–VIS spectroscopy suggests that the synthesized nanostructures show strong absorption in the UV range for all the samples. Fluorescence images of a single belt of S2 clearly show different colors along the length of the belt, which is attributed to different defects along the length of the belt. A single belt based UV sensor was highly sensitive to UV light.

References

1. Z.R. Dai, Z.W. Pan, Z.L. Wang, Adv. Funct. Mater. **13**, 9 (2003)
2. Z.W. Pan, Z.R. Dai, Z.L. Wang, Science **291**, 1947 (2001)
3. M.H. Wong, A. Berenov, X. Qi, M.J. Kappers, Z.H. Barber, B. Illy, Z. Lockman, M.P. Ryan, J.L. MacManus-Driscoll, Nanotechnology **14**, 968 (2003)
4. H. Hu, X. Huang, C. Deng, X. Chen, Y. Qian, Mater. Chem. Phys. **106**, 58 (2007)
5. F. Ahmed, S. Kumar, N. Arshi, M.S. Anwar, S.N. Heo, B.H. Koo, Acta Mater. **13–14**, 5190 (2012)
6. S. Polarz, A. Roy, M. Lehmann, M. Driess, F.E. Kruis, A. Hoffmann, P. Zimmer, Adv. Funct. Mater. **17**, 1385 (2007)
7. U. Manzoor, D.K. Kim, Physica E, Low-Dimens. Syst. Nanostruct. **41**, 500 (2009)
8. M.H. Huang, S. Mao, H. Feick, H. Yan, Y. Wu, H. Kind, E. Weber, R. Russo, P. Yang, Science **292**, 1897 (2001)
9. H.W. Ra, K.S. Choi, J.H. Kim, Y.B. Hahn, Y.H. Im, Small **4**, 1105 (2008)
10. J.S. Jeong, J.Y. Lee, J.H. Cho, H.J. Suh, C.J. Lee, Chem. Mater. **17**, 2752 (2005)
11. J.Q. Hu, Y. Bando, J.H. Zhan, Y.B. Li, T. Sekiguchi, Appl. Phys. Lett. **83**, 4414 (2003)
12. U. Manzoor, D.K. Kim, Scr. Mater. **54**, 807 (2006)
13. G.D. Yuan, W.J. Zhang, J.S. Jie, X. Fan, J.X. Tang, I. Shafiq, Z.Z. Ye, C.S. Lee, Adv. Mater. **20**, 168 (2008)
14. Z.L. Wang, J. Phys. Condens. Matter **16**, R829 (2004)
15. S.S. Shinde, P.S. Shinde, Y.W. Oh, D. Haranath, C.H. Bhosale, K.Y. Rajpure, Appl. Surf. Sci. **258**, 9969 (2010)
16. A.B. Djurisic, Y.H. Leung, Small **8**, 944 (2006)
17. W.J. Li, E.W. Shi, W.Z. Zhong, Z.W. Yin, J. Cryst. Growth **203**, 186 (1999)
18. R. Yousefi, B. Kamaluddin, Appl. Surf. Sci. **255**, 9376 (2009)
19. K. Kapoor, D. Lahiri, S.V.R. Rao, T. Sanyal, B.P. Kashyap, Bull. Mater. Sci. **27**, 59 (2004)
20. M. Dabiran, S.M. Seutter, P.I. Cohen, Surf. Rev. Lett. **5**, 783 (1998)
21. B.E. Sernelius, K.F. Berggren, Z.C. Jin, I. Hamberg, C.G. Granqvist, Phys. Rev. B **37**, 10244 (1988)
22. R. Wang, L.L.H. King, A.W. Sleight, J. Mater. Res. **11**, 1659 (1996)
23. D.G. Thomas, J. Phys. Chem. Solids **15**, 86 (1960)
24. V. Srikant, D.R. Clarke, J. Appl. Phys. **83**, 5447 (1998)
25. M. Lannoo, J. Bourgoin, *Point Defects in Semiconductors I: Theoretical Aspects* (Springer, Berlin, 1981)
26. M. Lannoo, J. Bourgoin, *Point Defects in Semiconductors II: Experimental Aspects* (Springer, Berlin, 1983).
27. F. Oba, S.R. Nishitani, S. Isotani, H. Adachi, J. Appl. Phys. **94**, 824 (2001)
28. A. Janotti, C.G. Van de Walle, Rep. Prog. Phys. **72**, 126501 (2009)
29. C. Soci, A. Zhang, B. Xiang, S.A. Dayeh, D.P.R. Aplin, J. Park, X.Y. Bao, Y.H. Lo, D. Wang, Nano Lett. **7**, 1003 (2007)
30. J. Suehiro, N. Nakagawa, S. Hidaka, M. Ueda, K. Imasaka, M. Higashihata, T. Okada, M. Hara, Nanotechnology **17**, 2567 (2006)